High-entropy gradient filler metal enables high-strength joints of Ti_2AlNb and GH4169 superalloy

Yinchen Wang[a, 1], Zhijie Ding[a, 1], Bin Wang[a], Zhenyang Zhang[a], Zhiwei Qin[a, *], Jia Yao[a], Yu Sun[a], Fengyun Yu[a], Honggang Dong[a], Peng Li[a, *]

[a] School of Materials Science and Engineering, Dalian University of Technology, Dalian 116024, PR China

1 These authors contributed equally to this work

*Corresponding authors. E-mail address: lipeng2016@dlut.edu.cn; qinzw@dlut.edu.cn

Contents

Note 1 Material characterization methods

The Ti_2AlNb and GH4169 base metals were sequentially polished using 80#, 400#, and 800# abrasive papers, followed by ultrasonic cleaning in anhydrous ethanol at 25 ^{o}C for 10 min. The crystal structures of the two filler metals were characterized using an Advance-type Bruker X-ray diffraction instrument (XRD), and the thermal behavior of the brazing foils was analyzed using a TGA/DSC3+ differential thermal analyzer (DTA) at a heating rate of 10 ^{o}C/min. Qualitative and quantitative compositional analyses of the alloying elements in each zone of the joints were carried out using a JXA-8530F PLUS field emission electron probe (EPMA, Electron probe micro-analyzer) equipped with a Wavelength dispersive spectrometer (WDS, Wavelength dispersive spectrometer). The scanning transmission electron microscope (STEM, JEOL JEM-2100F) samples were acquired by the focused ion beam (FIB, Helios G4 UX), and the crystal structure, lattice realationships and strain distribution were determined from the transmission electron microscopy (TEM) results. The microstructure of joints, fracture paths of joints, and fracture morphology of joints were observed using a field emission scanning electron microscope (SEM, Scanning electron microscope) type IT800-SHL. The nanohardness and elasticity modulus of the interfacial zone of joints were determined using a nanoindentation tester (TI 950 TriboIndenter) with the load set at 8 mN and the indentation spacing set at 5 μm.

Note 2 MD simulation

Molecular dynamics (MD) calculations were performed using the Large-scale Atomic/Molecular Massively Parallel Simulator (LAMMPS)[1]. Models of $(Ti, Zr)_2(Ni, Cu)/(Ti, Zr)(Ni, Cu)_3$ and $(Ni, Cr, Fe)_{ss}/(Ni, Cu, Fe, Cr)_{ss}$ interfaces were built. The atomic potential was developed by Zhou and Deluigi et al.[23], which was used in $(Ti, Zr)_2(Ni, Cu)/(Ti, Zr)(Ni, Cu)_3$ and $(Ni, Cr, Fe)_{ss}$ and $(Ni, Cu, Fe, Cr)_{ss}$ simulations. This work was carried out by randomly doping the original $Ti_2Ni/TiNi_3$ and Cr_{ss}/Ni_{ss} models. For the $(Ti, Zr)_2(Ni, Cu)$ atomic configuration, Zr atoms were randomly substituted for Ti atoms at a 51% rate, while Cu atoms were randomly substituted for Ni atoms at a 40% rate. For the $(Ti, Zr)(Ni, Cu)_3$ atomic configuration, Zr atoms were randomly substituted for Ti atoms at a rate of 49%, while Cu atoms were randomly substituted for Ni atoms at a rate of 53%. The $(Ti, Zr)_2(Ni, Cu)$ and $(Ti, Zr)(Ni, Cu)_3$ atomic configurations were based on points 1 and 2 in Table S8, respectively. For the $(Ni, Cr, Fe)_{ss}$ atomic configuration, Ni and Fe atoms were randomly substituted for Cr atoms at rates of 25% and 9%, respectively. For the $(Ni, Cu, Fe, Cr)_{ss}$ atomic configuration, Cu, Cr, and Fe atoms were randomly substituted for Ni atoms at 19%, 14%, and 16% respectively. The $(Ni, Cu, Fe, Cr)_{ss}$ and $(Ni, Cr, Fe)_{ss}$ atomic configurations were based on points 1 and 2 in Table S9, respectively. The $(Ti, Zr)_2(Ni, Cu)/(Ti, Zr)(Ni, Cu)_3$ model was oriented with its (100), (010), and (001) planes aligned, respectively, with the x-, y-, and z-axes, to create 19200 atoms. The $(Ni, Cr, Fe)_{ss}/(Ni, Cu, Fe, Cr)_{ss}$ model was oriented with its (100), (010), and (001) planes aligned, respectively, with the x-, y-, and z-axes, to create 16640 atoms. The

Conjugate Gradient (CG) method for energy minimization could reduce the internal stress of the structure, eliminate unreasonable atomic configurations during modeling, and put the atoms in a more balanced state, resulting in more accurate mechanical test results. Thus, the model was then subjected to energy minimization using the CG method. The Nose-Hoover thermostat method was commonly used to maintain the temperature stability of the system, ensuring that the system remained at the preset temperature during the energy minimization process and preventing uncontrolled temperature changes that could affect the energy. The relaxation of two interface models was carried out under isothermal and isobaric conditions (NPT ensemble) at 300 K. A global model was employed for relaxation to ensure computational accuracy. The simulated environment temperature increased from 300 K to 923 K within 50 ps. After the entire model was maintained at 923 K for 10 picoseconds, the tensile process was taken. A total of 250 ps during the tensile process was taken. The time step for the relaxation and subsequent stretching processes of the entire model was set to 0.001 ps. Uniaxial tension was performed under an NVT ensemble, and the temperature was controlled at 300 K. Periodic boundary conditions were maintained along all orientations. In order to achieve uniaxial tension, the strain rate was set to 1 $\times 10^9$/s. OVITO[4] was used to visualize atomic configurations and analyze simulation results.

Note 3 Modelling of residual stress

The finite element analysis (FEA) modelling method was chosen to simulate the residual stresses generated during the brazing process. The computation was conducted using the ABAQUS/Standard (or ABAQUS/Explicit) solver. The 3D geometry, matching the dimensions of the actual brazed joint, was modeled in ABAQUS/CAE. The properties of GH4169 alloy and Ti_2AlNb alloy used in this paper are consistent with those reported in References 1-3[567]. The properties of $(TiZrHf)_{50}(NiCu)_{45}Al_5$ and $(TiZrHf)_{30}(NiCu)_{65}Al_5$ filler metals considered for the simulation of residual stress are summarized in Table S1 using Jmat Pro 12.0 software. Residual stresses developed in the joint as soon as solidification of the brazed interlayer began, leading to the GH4169, Ti_2AlNb, and filler metals behaving as a fully connected body. The following boundary conditions were applied during the finite element simulation. Brazing alloy, Ti_2AlNb, and GH4169 alloy were all assumed to be isotropic materials. Among these, the brazing alloy exhibited only elastic deformation, while Ti_2AlNb and GH4169 alloy showed elastoplastic deformation. The upper and lower surfaces of the filler metal were coplanar with the Ti_2AlNb alloy and GH4169, respectively. Atomic diffusion and interfacial chemical reactions between the brazing alloy and the base metals on both sides were not considered. The brazed joint was constrained to ensure that the brazing alloy maintained tight contact with both base metals throughout the brazing process, with no defects present at their interface. The bottom surface of the model was fixed, while the entire top surface was applied with 0.1 MPa pressure, consistent with the brazing

process. The temperature boundary conditions were set to heat from room temperature (25 °C) at a rate of 10 °C/min to brazing temperature, followed by a 15-min holding period at brazing temperature, consistent with the actual brazing process conditions. The paper conducted the FEA for both single filler metal and HGFM at a temperature of 1065 °C. In addition, the FEA using HGFM for the joints at 1035°C and 1080°C was also conducted. The heat transfer mechanisms during the cooling process were thermal radiation and thermal convection. The residual stress simulation was carried out in the cooling temperature regime of brazing temperature to 25 °C (room temperature), coupling the thermal and mechanical responses of the joint. This paper adopted the C3D8R mesh grid classification scheme. Based on the residual stress distribution characteristics of brazed joints (primarily concentrated in the braze seam and its adjacent regions), a non-uniform mesh division scheme was implemented. A finer mesh was applied in the stress concentration zones near the interface to enhance the accuracy of residual stress calculations. Areas farther from the interface were divided into a sparser coarse grid. It effectively reduced the total number of mesh elements while controlling the relative error in stress calculations for key regions, significantly improving computational efficiency. The model was presumed to follow the elastic strain-stress correlation by obeying the isotropic Hooke's law. The scattering of residual stress for the brazed joint models was comprehended by the distribution of von Mises-stress across the entire joint. Additionally, the residual stress on path geometry along and across the joining interface was simulated in order for better insight into the distribution and the consequences.

From an experimental perspective, this paper employed an XL-640 stress measuring instrument to determine residual stresses of brazed joints using GHFM and a single brazing filler metal $(TiZrHf)_{50}(NiCu)_{45}Al_5$. An Mn target was used during the measurement process, with a collimator diameter of 1 mm. Stress calculations were performed using the 2θ method, with peak shape processing conducted via the Pearson VII method. Under each brazing condition, at least three residual stress values were measured to determine the average value. The stress test results showed that compared to using a single filler metal, the maximum residual stress at the joint when using HGFM was decreased from 94.2 ± 15.5 MPa to 72.8 ± 1.3 MPa, consistent with the trend of the simulation.

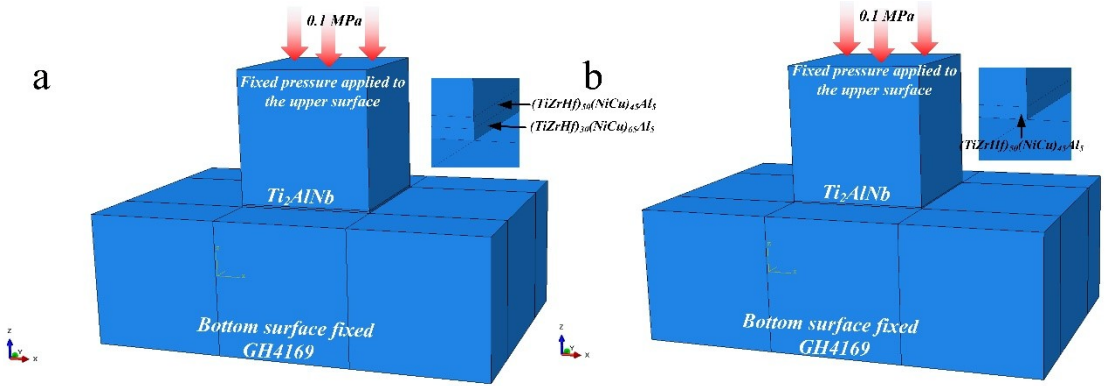

Fig. S1. Models and boundary conditions for brazed joints.

Table S1 Properties of the filler metals

Filler metal	Temperature (°C)	Conductivity (W/(m·K))	Density (g/cm³)	Expansion coefficient (%)	Specific heat (J/(mol·K))
$(TiZrHf)_{50}(NiCu)_{45}Al$	25	21.37	~8.25	0	26.43
	100	23.27		0.13	27.31
	200	24.56		0.21	28.74
	300	25.73		0.31	30.31
	400	26.83		0.41	32.19
	500	27.91		0.54	34.63
	600	29.03		0.68	38.10

	700	30.31		0.84	44.02
	800	32.18		1.03	61.56
	900	37.40		1.33	68.06
	1000	44.88		1.76	33.87
	1100	46.72		2.02	34.94
	1200	48.48		2.29	35.99
$(TiZrHf)_{30}(NiCu)_{65}Al_5$	25	34.21	~8.33	0	7.38
	100	36.08		0.08	7.56
	200	38.46		0.20	7.92
	300	40.78		0.32	8.28
	400	43.06		0.44	8.64
	500	45.28		0.56	9.00
	600	47.42		0.68	9.36
	700	49.47		0.81	9.54
	800	51.52		0.96	19.44
	900	47.51		2.17	65.52
	1000	47.30		2.73	59.76
	1100	48.93		2.95	10.08
	1200	50.59		3.26	10.26

Note 4 Microstructure evolution of the hybrid joint with GHFM

The backscattered electron images of joints at different brazing temperatures (Fig. S1) suggested that the changes in microstructure were primarily observed in the central region of the brazing seam. This region was mainly composed of grey-white phases labelled as P1, P4 and P5, a black phase labelled as P2 and a bright white phase labelled as P3. The black block-like phase labelled as P2 contained primarily Ti, Zr, Al, Cu, and Ni elements. The total content of Ti and Zr elements was 18.97 at.%, Al content was 16.87 at.%, and the total content of Ni and Cu elements was 58.75 at.%. Combining relevant papers [8] and Al-Ni(Cu)-Ti(Zr) ternary phase diagrams [9], phase P2 was inferred to be the Al(Ti, Zr)(Ni, Cu)$_2$ phase.

With increasing brazing temperature, the bright white phase (Ti, Zr, Hf)(Ni, Cu) and the black phase Al(Ti, Zr)(Ni, Cu)$_2$ gradually decreased, while the grey-white phase (Ti, Zr, Hf)(Ni, Cu, Al) increased gradually. When the brazing temperature reached 1065 ^{o}C, the mutual diffusion and metallurgical reactions between the GHFM and the adjacent base metals became more thorough, almost disappearing the bright white phase. The interfacial microstructure in the central region became more uniform, forming a region mainly composed of (Ti, Zr, Hf)(Ni, Cu, Al) phase. As the brazing temperature rose to 1080 ^{o}C, phase transformation occurred in the Ti_2AlNb base metal, which led to noticeable dissolution phenomena, resulting in coarsening of the microstructure. Through statistical analysis in Fig. S1f, as the brazing temperature increased from 1020 ^{o}C to 1065 ^{o}C, the overall thickness of the brazing seam increased from 50.9 μm to 74.3 μm. With a further increase in temperature to 1080 ^{o}C,

the overall thickness of the brazing seam increased to 124.9 μm, primarily due to the phase transformation and significant dissolution of the Ti_2AlNb base metal, resulting in a sharp increase in seam thickness.

Thus, elemental diffusion and metallurgical reactions occurred at the interface, leading to significant phase transitions and increased thickness of the reaction layer, which revealed that brazing temperature was a crucial factor affecting interfacial microstructure and mechanical properties of joints.

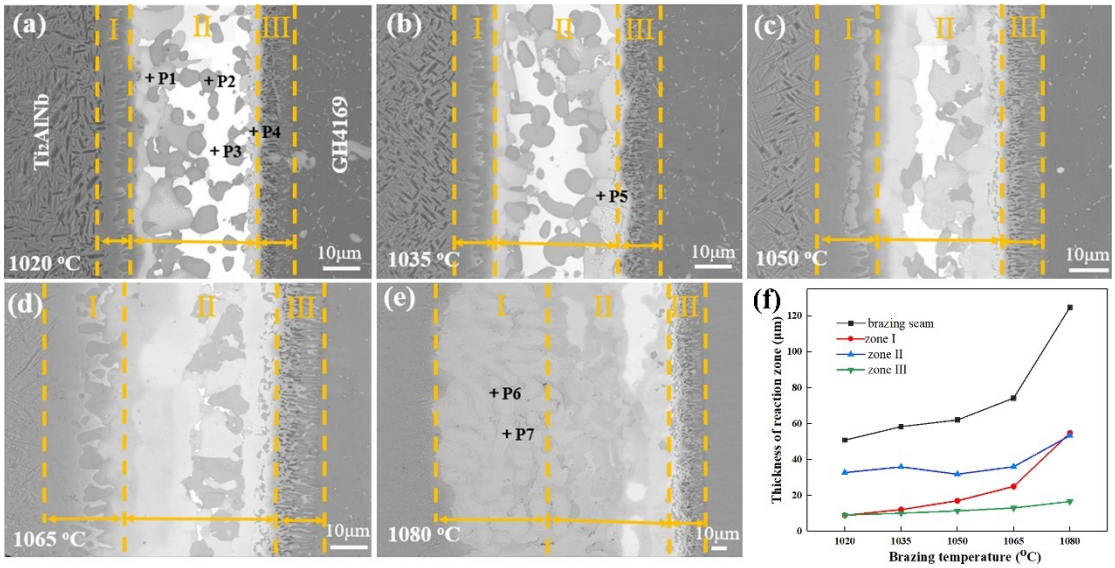

Fig. S2. Interfacial microstructure evolution and thickness variation of joints brazed under different brazing temperatures for 15 min with GHFM.

Table S2 Widths of each zone at different brazing temperatures.

Brazing temperatures	Width of different zones (mm)			
	I	II	III	Brazing seam
1020 °C	9.0	32.8	9.1	50.9
1035 °C	12.2	36.0	10.2	58.4
1050 °C	17.1	31.9	11.5	62.1
1065 °C	25.1	36.1	13.1	74.3
1080 °C	54.8	53.4	16.7	124.9

Table S3 EPMA analysis results (at.%) of the marked locations in Fig. S2.

Locations	Al	Ti	Cr	Fe	Ni	Cu	Zr	Nb	Hf	Possible phase
P1	8.07	17.58	2.89	3.39	29.88	13.32	7.81	10.63	6.44	(Ti, Zr, Nb) (Ni, Cu, Al)
P2	16.87	10.42	0.19	0.80	38.01	20.74	8.55	0.23	4.18	Al(Ti, Zr)

										$(Ni, Cu)_2$
P3	1.49	12.78	0.08	0.48	40.91	19.60	10.78	1.55	12.35	(Ti, Zr, Hf) (Ni, Cu)
P4	5.35	14.82	5.14	6.47	34.76	10.36	7.52	9.56	6.03	(Ti, Zr, Hf, Nb) $(Ni, Cu, Al)_2$
P5	8.75	18.61	2.00	2.73	29.34	14.98	9.78	7.32	6.50	(Ti, Zr, Hf, Nb) (Ni, Cu, Al)
P6	13.24	34.92	0.54	0.86	19.59	4.11	1.82	24.27	0.64	Ti_2AlNb $+(Ni, Cu)_{ss}$
P7	12.74	49.51	0.62	0.69	2.32	1.48	0.63	31.48	0.54	β/B2

To have a deeper understanding of the element distribution of joints, further EPMA mapping was performed of joints brazed at 1065 °C and 1080 °C, as depicted in Figs. S3 and S4. At 1065 °C, there was a gradient distribution of Ti, Al, and Nb elements from the Ti_2AlNb side to the central brazed seam. Ti was distributed in Zones I and II, and a small amount in Zone III. With the dissolution of the Ti_2AlNb base metal, the element Al diffused into the central region under the effect of the elemental concentration gradient. Thus, there was a distribution of Al elements in both Zones I and II of the brazing seams. Nb was mainly distributed in the diffusion-affected zone near the Ti_2AlNb substrate. Ni had a higher elemental content in GHFM and was the main element of GH4169 alloy, and its distribution was similar to Ti elements, which mainly existed in Zones II and III close to the GH4169 side, and had a tendency to extend into the diffusion Ti_2AlNb side. Zr, Hf, and Cu, being primary components of the GHFM, exhibited higher and more uniform distribution in Zone I. The black blocky phase was enriched in elements such as Al, Ni, Cu, and Zr, indicating a strong affinity between these elements based on the mixing enthalpy values in Table S4. Fe and Cr were mainly distributed in the diffusion reaction region near the GH4169 side, with lower concentrations in the brazing seam, suggesting lower diffusion coefficients during the brazing process. Zones with higher Fe and Cr

concentrations exhibited a Ni content depletion. At 1080 °C, severe dissolution of the Ti_2AlNb substrate was observed, leading to a sharp increase in the diffusion of Ti_2AlNb alloy elements towards the brazed seam.

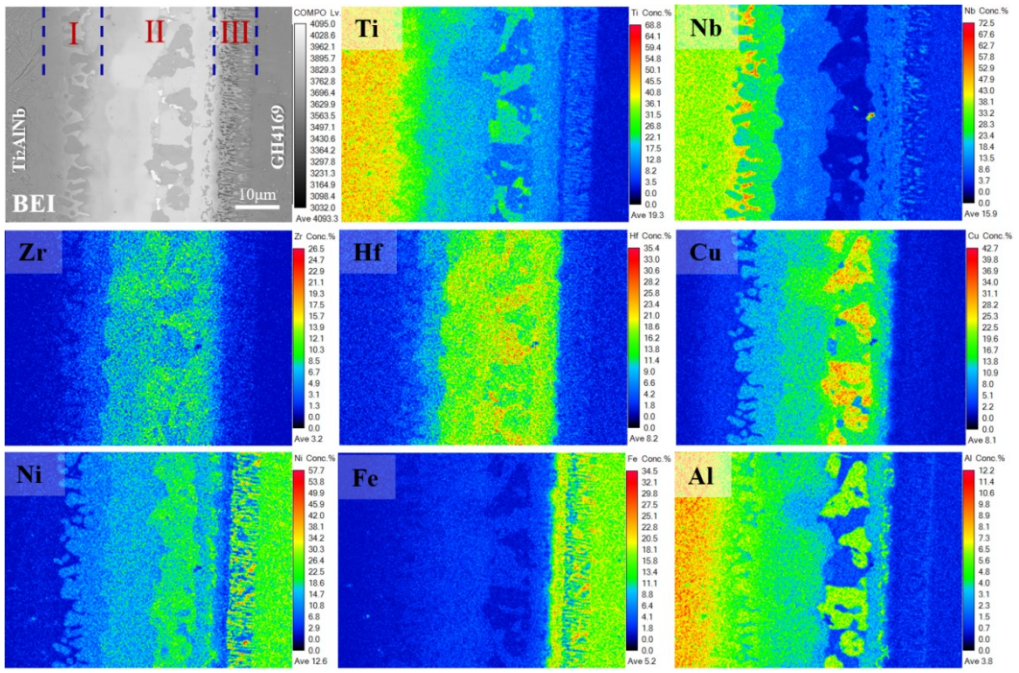

Fig. S3. Elemental distribution in the interfacial zone of the brazed joint at 1065 °C for 15 min with GHFM.

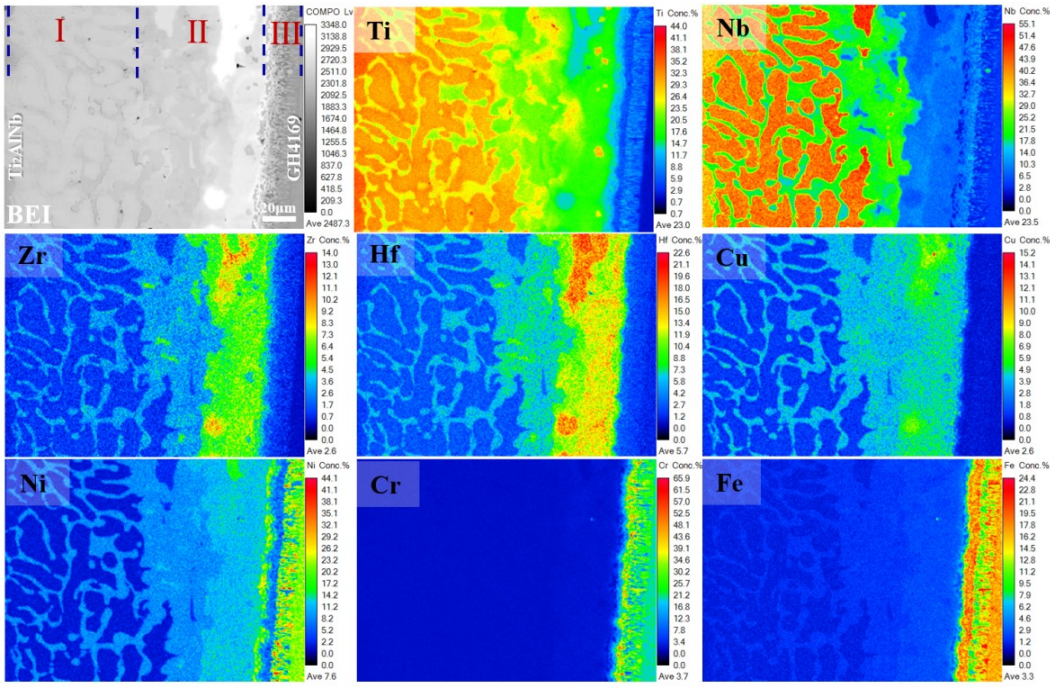

Fig. S4. Elemental distribution in the interfacial zone of the brazed joint at 1080 °C for 15 min with GHFM.

Note 5 Growth kinetics of interfacial microstructure at the hybrid joint

To investigate the effect of brazing temperature on the diffusion behaviors from a kinetics perspective, the relationship between brazing temperature, reaction layer thickness, and the growth activation energy was determined by the following Equations S1-S3 [101112].

$$w^2 = kt \tag{1}$$

$$k = k_0 exp\left(\frac{-Q}{RT}\right) \tag{2}$$

$$lnw = \frac{1}{2}lnk_0 t - \frac{Q}{2RT} \tag{3}$$

w is the thickness of the reaction layer (μm), k is the growth rate ($\mu m^2 \cdot s^{-1}$), and t is the brazing holding time (s). k_0 is the growth rate constant, R is the ideal gas constant, which is equal to 8.314 $kJ \cdot mol^{-1} \cdot K^{-1}$, T is the brazing temperature (K), and Q is the growth activation energy (kJ/mol). The sluggish diffusion effect of GHFM at lower brazing temperatures increased diffusion resistance and reduced diffusion rates, resulting in slower growth of the interfacial thickness [13]. Based on Fig. S5c, the growth activation energy for the $(Ni, Cr, Fe)_{ss}$ phase in brazing Zone III was relatively low, measured at 232.5 $kJ \cdot mol^{-1} \cdot K^{-1}$. Conversely, the growth activation energy for the Ti_2AlNb phase solid-solutioned with Ni and Cu elements and the B2 phase in Zone I was relatively higher, attributed to the higher diffusion activation energy resulting from the high plastic deformation flow stress values of the Ti_2AlNb substrate.

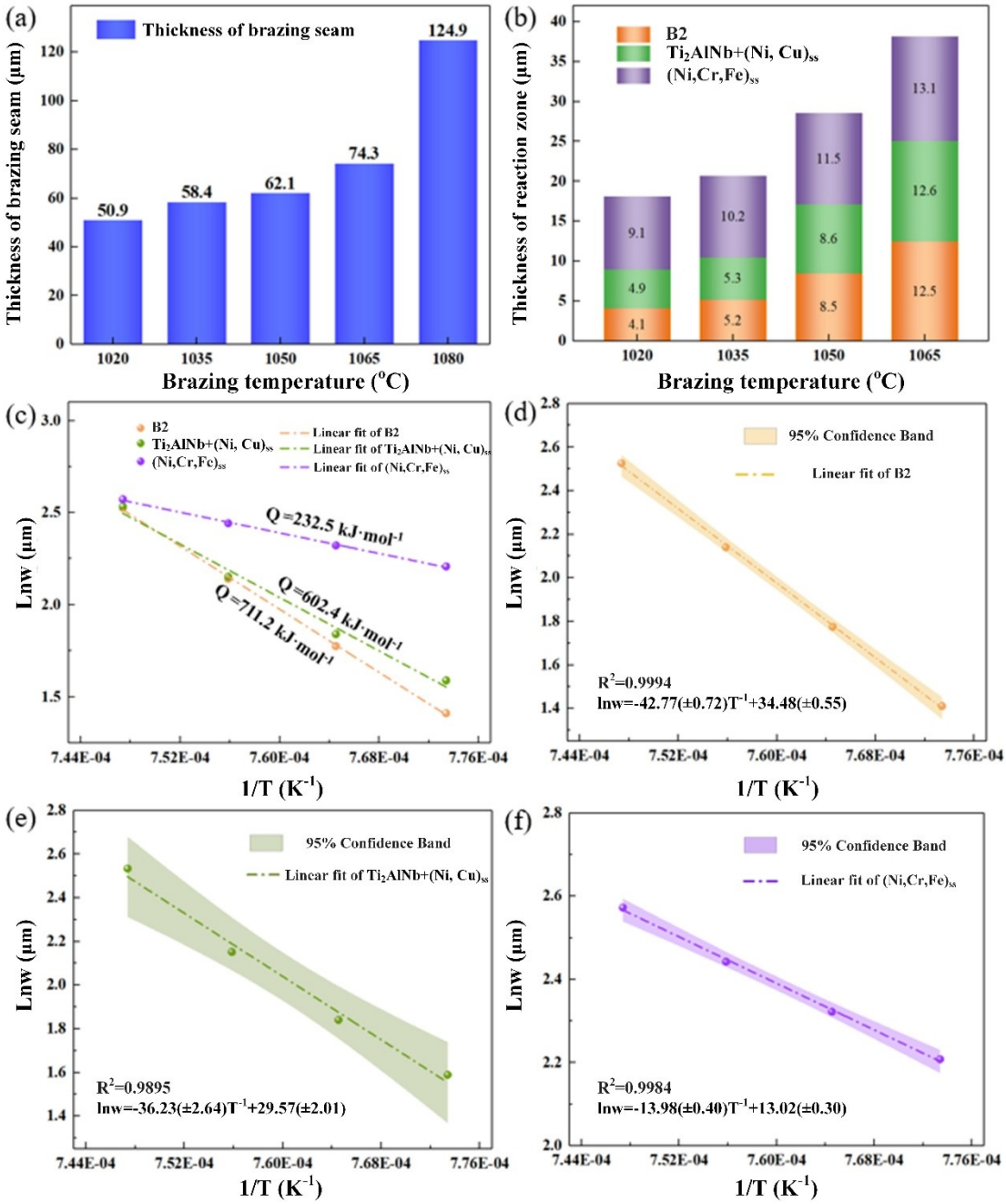

Fig. S5. The relationships between the thickness of the reaction layers and the brazing temperature. (a) The thickness of the brazing seam; (b) thickness of reaction layer; (c) activation energy; (d-f) the correlation between reaction layer *lnw* and *1/T*.

Table S4 Widths of the interface by Li et al..

Brazing temperatures	Width of the interface (mm)			
960 °C	125.60	129.62	129.63	128.28
980 °C	166.76	168.72	167.62	167.70
1000 °C	213.70	211.82	212.25	212.59
1020 °C	202.27	206.58	197.58	202.14

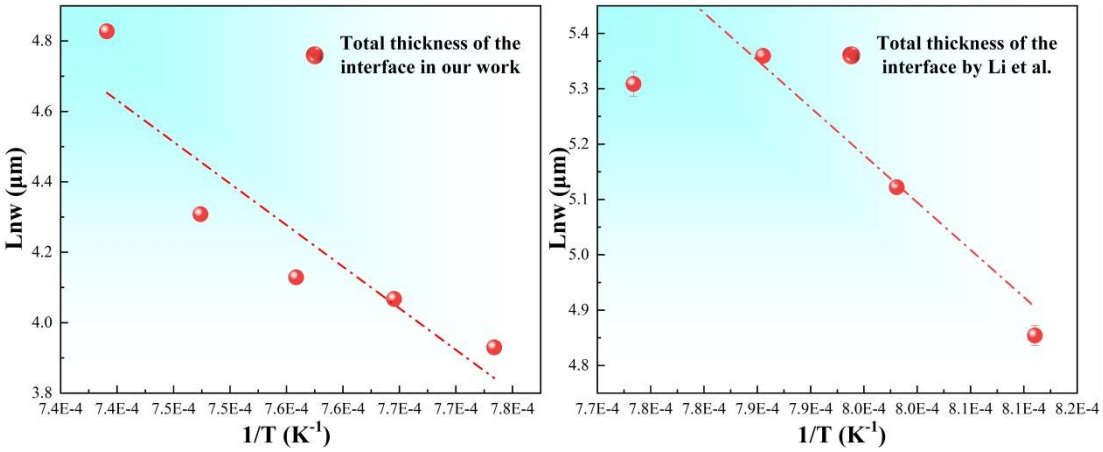

Fig. S6. Activation energy of the interface in our work and activation energy of the interface by Li et al..

Note 6 Microstructure evolution of joint with GHFM

The formation of the interfacial microstructure of joints begins with the diffusion of elements and interfacial reactions, including solid-state diffusion between atoms, liquid-phase diffusion and metallurgical reactions, isothermal solidification processes, and reactive phase growth and microstructureal evolution. In order to visually describe the interfacial tissue evolution mechanism of joints during brazing, a simplified schematic diagram is shown in Fig. S7.

During the brazing process, the assembly was carried out in the manner shown in Fig. S7a. When the brazing temperature was higher than the glass transition temperature of the amorphous filler metal, close physical contact occurred between the base material and the filler metal on both sides, and solid-state diffusion of atoms occurred at the interface as the temperature rose. Upon reaching the liquidus temperature of the brazing filler, it started melting and fully wets both base materials. Facilitated by concentration gradients, elements such as Ti, Al, and Nb from the Ti_2AlNb alloy and Ni, Cr, and Fe from the GH4169 alloy diffused into the molten brazing filler. The Ti and Al elements from the liquid brazing filler diffused to the GH4169 side, while Zr, Hf, and Cu elements diffused to both base materials. The interaction between the liquid brazing filler and the base material elements formed a thin diffusion reaction layer at the interface, as shown in Fig. S7b.

As the temperature rose to the brazing temperature and was maintained during the holding stage, more thorough elemental diffusion occurred between the two base materials and the liquid brazing filler. Ti and Nb elements from the Ti_2AlNb alloy

diffused into the brazing filler, elevating its melting temperature and initiating the isothermal solidification process, resulting in the formation of layered structures of varying degrees near the Ti_2AlNb alloy. Ni and Cu elements from the brazing filler diffused to the Ti_2AlNb alloy side, forming a phase dissolved with Ni and Cu elements. Nb, Ni, and Cu elements, being stabilizing elements for the β phase, promoted the nucleation and growth of β-Ti, generating a continuous B2 phase on the Ti_2AlNb side. The reaction between the brazing filler and the elements from both base materials formed gray (Ti, Zr, Hf)(Ni, Cu, Al), black Al(Ti, Zr)$(Ni, Cu)_2$, and bright white (Ti, Zr, Hf)(Ni, Cu) phases in the central zone of the brazing seam, as depicted in Fig. S7c.

With further increase in brazing temperature, the entry of Ti, Al, and Ni elements into the brazing seam increased, leading to more uniform diffusion of brazing filler elements within the brazing seam. During cooling, a predominantly gray phase (Ti, Zr, Hf)(Ni, Cu) was formed in the central zone of the brazing seam, as shown in Fig. S7c. On the GH4169 alloy side, compared to elements such as Fe and Cr, Ni and Ti exhibited stronger affinity and were more prone to diffuse to the central zone of the brazing seam. The liquid brazing filler tended to diffuse Ti elements to the GH4169 side, while the diffusion capacity of elements such as Fe and Cr to the brazing seam was limited.

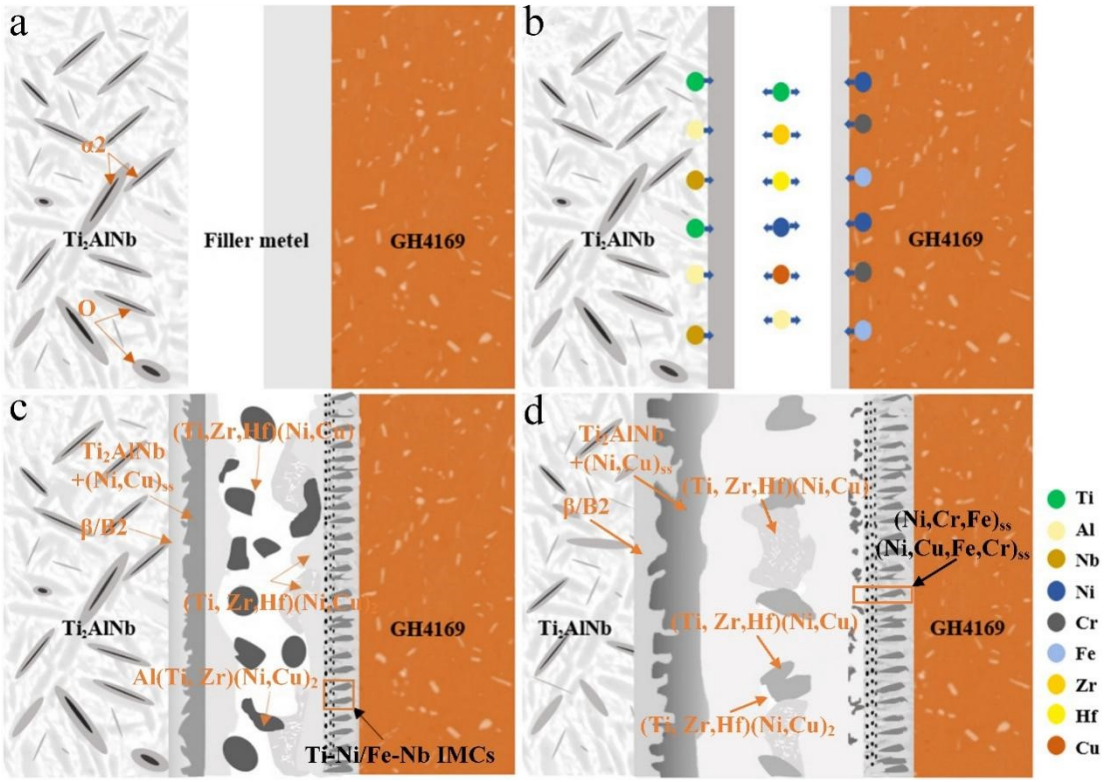

Fig. S7. Schematic of Ti_2AlNb/GH4169 brazed joint microstructure evolution process. (a) Physical contact, (b) filler melting and atomic diffusion, (c) formation of reaction phases and (d) growth and evolution of reaction phases.

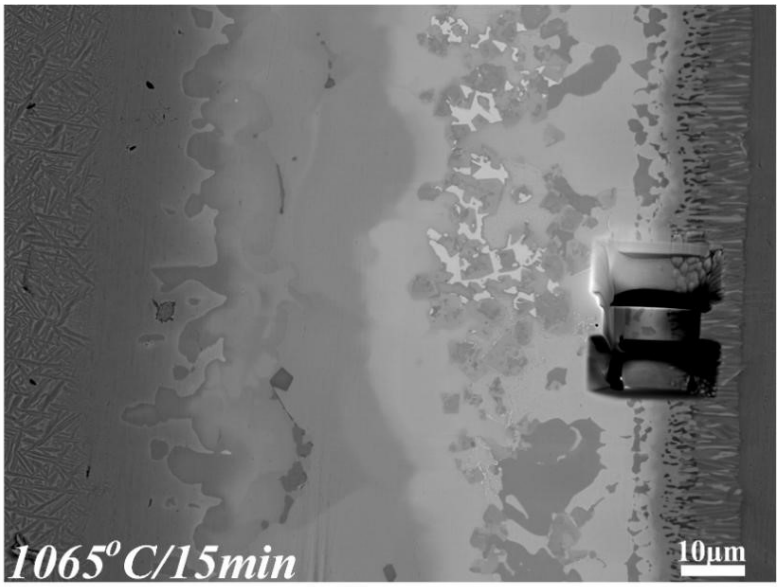

Fig. S8. FIB cutting location of joints at 1065 °C at 15 min with GHFM.

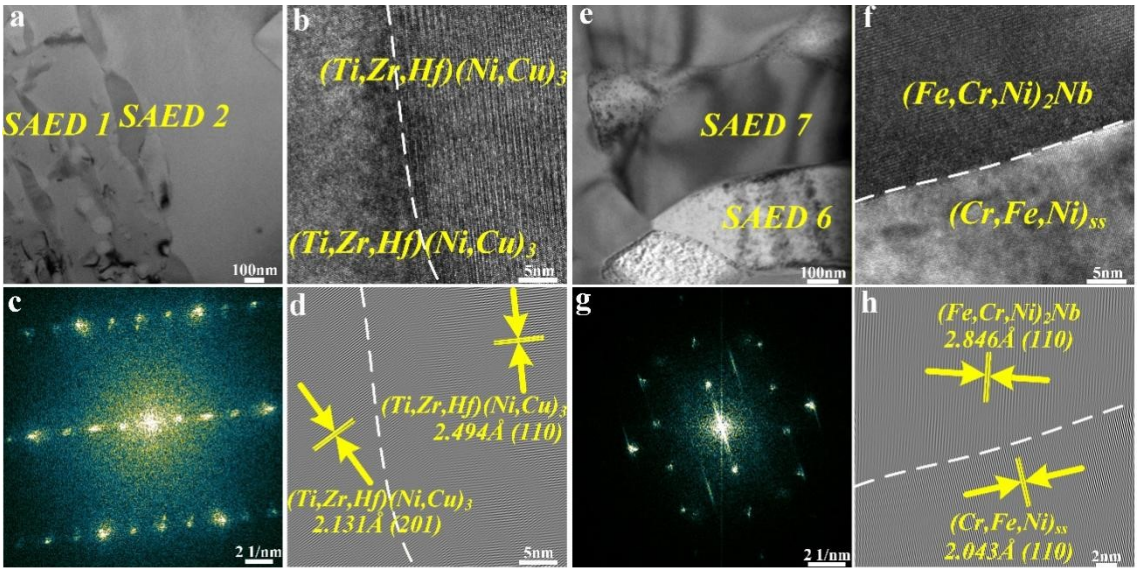

Fig. S9. Interfacial characteristics of joints brazed at 1020 ºC for 15 min with GHFM. (a) Lagered bright field images, (b) HRTEM image in Fig. S9a, (c) FFT image in Fig. S9b, (d) lattice fringe image in Fig. S9b, (e) Lagered bright field images, (f) HRTEM image in Fig. S9e, (g) FFT image in Fig. S9f, (h) lattice fringe image in Fig. S9f.

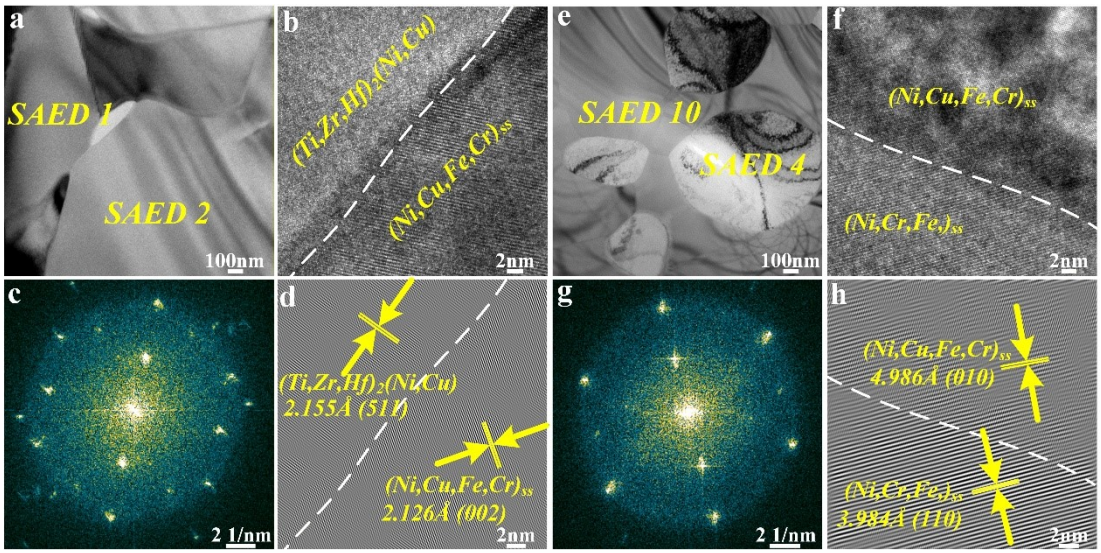

Fig. S10. Interfacial characteristics of joints brazed at 1065 °C for 15 min with GHFM. (a) Lagered bright field images, (b) HRTEM image in Fig. S10a, (c) FFT image in Fig. S10b, (d) lattice fringe image in Fig. S10b, (e) Lagered bright field images, (f) HRTEM image in Fig. S10e, (g) FFT image in Fig. S10f, (h) lattice fringe image in Fig. S10f.

Table S5. Statistics for the interfacial lattice misfit of the joint brazed at 1020 °C

Temperature	Lattice misfit of the interface			
	$(Ti,Zr,Hf)_2(Ni,Cu)$ /$(Ti,Zr,Hf)(Ni,Cu)_3$	$(Ti,Zr,Hf)(Ni,Cu)_3$ /$(Fe,Cr,Ni)_2Nb$	$(Ti,Zr,Hf)(Ni,Cu)_3$ /$(Ti,Zr,Hf)(Ni,Cu)_3$	$(Fe,Cr,Ni)_2Nb$ /$(Ni,Cr,Fe)_{ss}$
1020 °C	37.90%	48.32%	25.16%	33.23%

Table S6. Statistics for the interfacial lattice misfit of the joint brazed at 1065 °C

Temperature	Lattice misfit of the interface			
	$(Ni,Cu,Fe,Cr)_{ss}$ /$(Ni,Cr,Fe)_{ss}$	$(Ni,Cr,Fe)_{ss}$ /$(Ni,Cu,Fe,Cr)_{ss}$	$(Ti,Zr,Hf)(Ni,Cu)_3$ /$(Ni,Cu,Fe,Cr)_{ss}$	$(Ni,Cu,Fe,Cr)_{ss}$ /$(Ni,Cr,Fe)_{ss}$
1065 °C	3.72%	13.24%	18.53%	20.14%

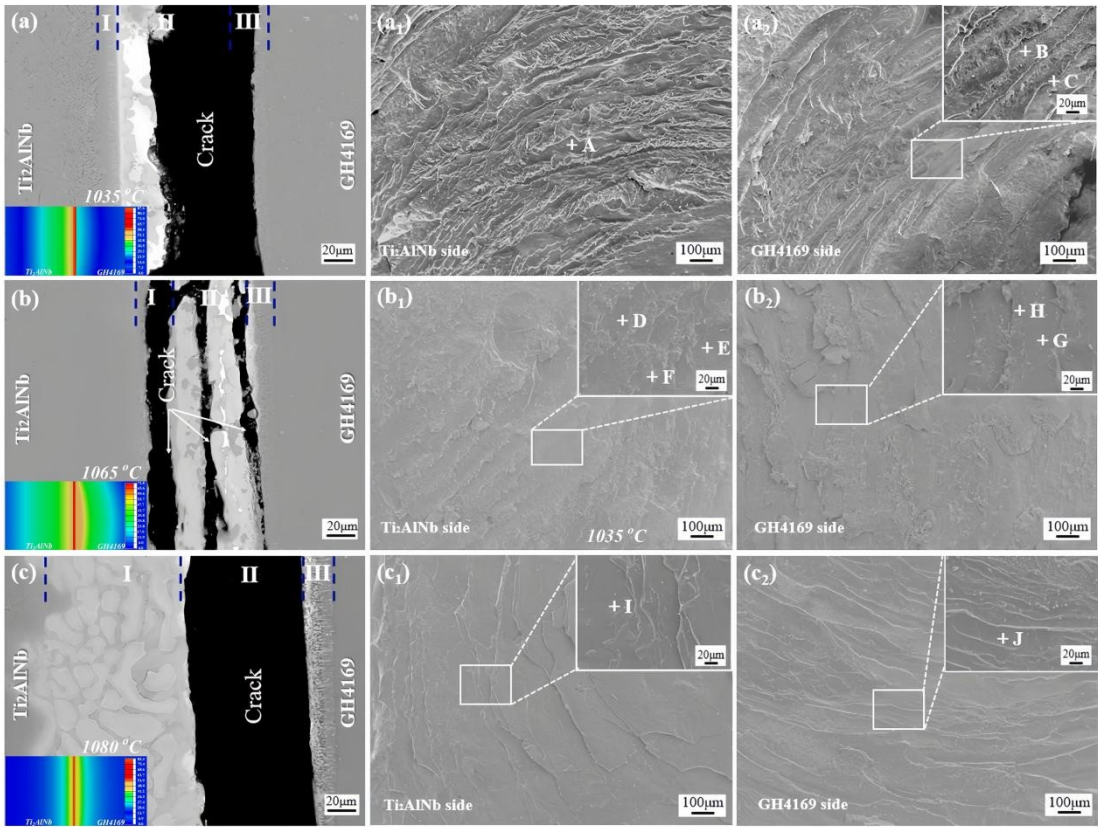

Fig. S11. Fracture characteristics and stress distribution of joints at different brazing temperatures at 15 min with GHFM. (a-c) The fracture path and stress distribution, (a_1-c_1) Ti_2AlNb side fracture morphology, (a_2-c_2) GH4169 side fracture morphology.

Table S7 EDS points analysis results (at.%) of the marked locations in Fig. S11.

Locations	Al	Ti	Cr	Fe	Ni	Cu	Zr	Nb	Hf	Possible phase
A	10.13	24.84	1.46	2.43	24.09	13.98	6.38	9.07	7.62	(Ti, Zr, Nb, Hf)(Ni, Cu, Al)
B	4.02	6.52	48.5	16.01	19.16	0.56	0.95	3.42	0.85	$(Ni, Cr, Fe)_{ss}$
C	3.69	10.32	16.26	19.76	31.56	1.98	5.83	2.58	8.04	$(Ni, Cr, Fe)_{ss}$
D	11.37	18.44	6.99	8.66	32.37	5.11	4.83	6.76	5.39	(Ti, Zr, Nb, Hf)$(Ni, Cu, Al)_2$
E	15.24	21.55	1.71	3.15	23.8	10.74	8.06	8.96	6.78	(Ti, Zr, Nb, Hf)(Ni, Cu, Al)
F	4.95	17.03	18.88	18.81	20.70	1.71	4.04	8.49	4.72	$(Ni, Cr, Fe)_{ss}$
G	12.04	19.45	2.91	4.85	27.44	8.50	7.16	10.04	7.61	(Ti, Zr, Nb, Hf) (Ni, Cu, Al)
H	12.47	23.30	1.74	3.18	25.15	11.17	6.34	9.13	7.51	(Ti, Zr, Nb, Hf) (Ni, Cu, Al)
I	17.42	35.42	1.74	1.94	16.95	6.18	2.30	15.57	2.48	Ti_2AlNb+ $(Ni, Cu)_{ss}$
J	2.28	10.51	29.68	20.64	22.27	0.12	2.04	7.88	2.05	$(Ni, Cr, Fe)_{ss}$

Result and discussion

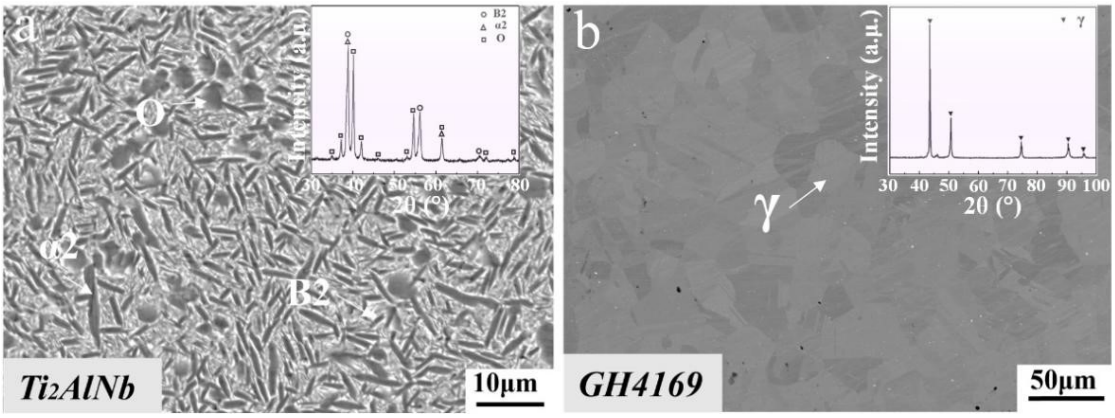

Fig. S12. Microstructure and XRD patterns of base metals.

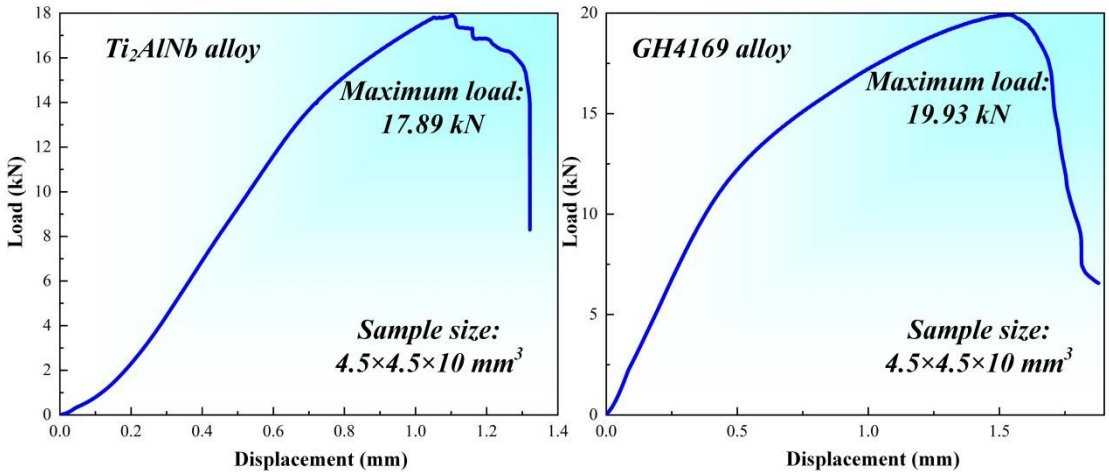

Fig. S13. Load-displacement curves of Ti_2AlNb alloy and GH4169 alloy.

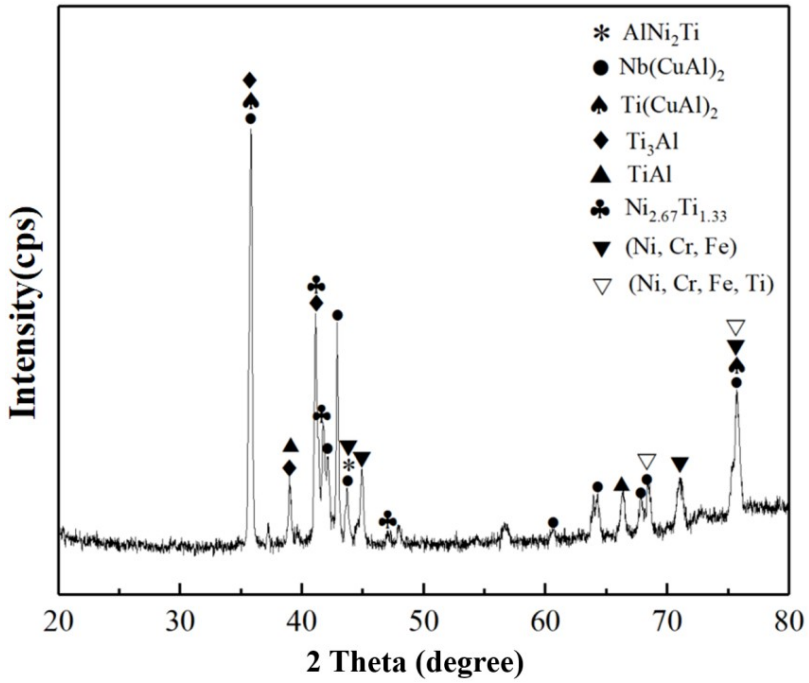

Fig. S14. XRD pattern of the fracture surfaces at the Ti_2AlNb side at 1065 ^{o}C.

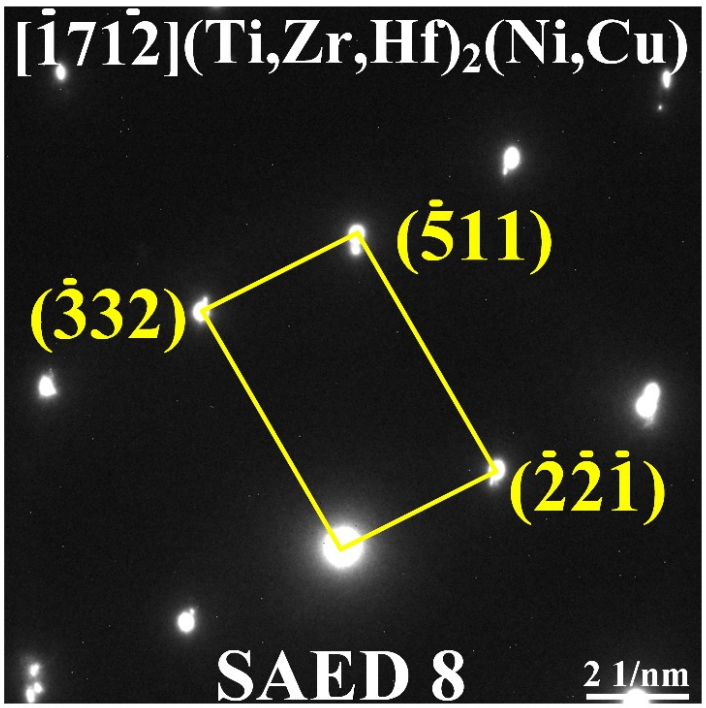

Fig. S15. SAED 8 pattern corresponding to the marked locations in Figs. 4d.

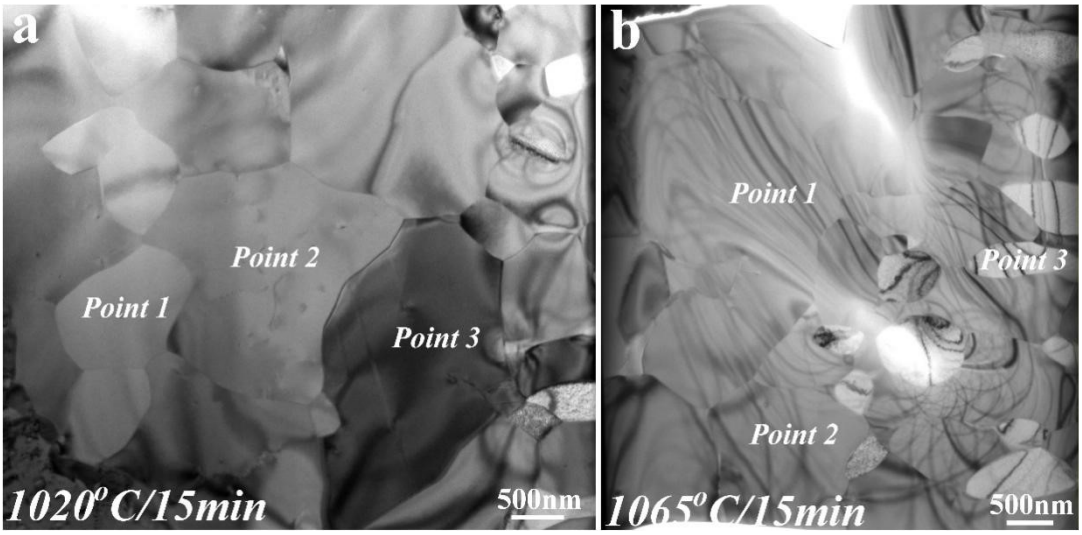

Fig. S16. TEM-EDS analysis results of the interface of joints.

Table S8 TEM-EDS analysis results (at.%) of the marked locations in Fig. S16

Locations	Ti	Zr	Hf	Nb	Ni	Cu	Fe	Cr	Al	Ω
Point 1	30.9	22.4	10.3	-	22.0	14.4	-	-	-	0.59
Point 2	12.0	5.2	6.3	-	35.8	28.5	-	-	12.2	0.71
Point 3	7.4	26.2	-	12.6	15.7	15.2	12.2	10.7	-	0.86

Table S9 TEM-EDS analysis results (at.%) of the marked locations in Fig. S16

Locations	Ti	Nb	Ni	Cu	Fe	Cr	Ω
Point 1	8.8	7.4	34.0	19.4	16.1	14.3	2.36
Point 2	-	-	25.4	-	8.9	65.7	1.84
Point 3	-	21.1	18.3	-	35.9	24.7	1.15

Table S10 Chemical composition of base metals (at.%)

Metal	Cr	Fe	Mo	Nb	Al	Ti	Ni
Ti_2AlNb	-	-	-	25.91	23.12	Bal.	-
GH4169	20.18	19.66	1.79	3.40	1.25	1.14	Bal.

Table S11 Enthalpy of mixing between elements ΔH_{mix} (kJ/mol)

	Ti	Zr	Hf	Ni	Cu	Al	Nb	Cr
Ti	-	-	-	-	-	-	-	-
Zr	0	-	-	-	-	-	-	-
Hf	0	0	-	-	-	-	-	-
Ni	-35	-49	-42	-	-	-	-	-
Cu	-9	-23	-17	4	-	-	-	-
Al	-30	-44	-39	-22	-1	-	-	-
Nb	2	4	4	-30	3	-18	-	-
Cr	-7	-12	-9	-7	12	-10	-7	-

Table S12 EPMA analysis results (at.%) of the marked locations in Fig. 2

Locations	Al	Ti	Cr	Fe	Ni	Cu	Zr	Nb	Hf	Possible phase
A	19.52	51.18	0.07	0.17	1.71	0.67	0.04	26.64	-	β/B2
B	15.62	30.88	0.39	1.14	22.64	8.60	1.81	18.36	0.55	Ti_2AlNb+ $(Ni, Cu)_{ss}$
C	1.26	12.59	0.06	0.53	42.19	21.22	8.91	1.65	11.59	(Ti, Zr, Hf) $(Ni, Cu)_2$
D	12.35	24.22	1.19	2.00	29.43	11.76	5.33	9.83	3.91	(Ti, Zr, Nb) (Ni, Cu, Al)
E	10.87	20.24	1.77	2.39	30.46	12.68	7.37	8.32	5.89	(Ti, Zr, Nb, Hf) (Ni, Cu, Al)
F	9.76	19.65	1.77	2.18	30.93	13.65	7.72	8.53	5.82	(Ti, Zr, Nb, Hf) (Ni, Cu, Al)
G	10.93	19.05	2.21	2.80	31.57	12.25	6.72	8.74	5.73	(Ti, Zr, Nb, Hf) (Ni, Cu, Al)
H	9.51	17.24	3.42	4.86	33.50	9.31	6.80	9.40	5.96	(Ti, Zr, Nb, Hf) (Ni, Cu, Al)
I	2.90	13.67	17.02	19.53	29.38	1.35	3.68	8.24	4.23	(Ni, Cr, $Fe)_{ss}$+(Ti, $Zr)_2$(Ni, Cu)
J	1.61	9.06	15.80	14.88	47.72	0.38	0.88	9.68	-	Ni-rich(Ni, Cr, $Fe)_{ss}$+(Ti, $Zr)_2$(Ni, Cu)
K	1.83	12.94	19.52	21.62	29.56	0.67	3.23	8.10	2.53	(Ni, Cr, $Fe)_{ss}$+ $(Ti, Zr)_2$(Ni, Cu)

Equation S4

$$\delta = \sqrt{\sum_{i=1}^{n} C_i\left(1 - \frac{r_i}{r}\right)^2}, \quad r = \sum_{i=1}^{n} C_i r_i \tag{4}$$

Equation S5

$$\Delta S_{mix} = -R\sum_{i=1}^{n}\left(C_i \ln C_i\right) \tag{5}$$

Equation S6

$$\Delta H_{mix} = 4\sum_{i=1, i\neq j}^{n} \Delta_{mix}^{AB} C_i C_j \tag{6}$$

Where n, c_i and r_i denote the count of principal elements, the atomic fraction and atomic radius of the i-th element, and the average atomic radius, respectively.

Equation S7

$$\Delta\mu_{mix} = \mu_{layer1} - \mu_{layer2} \tag{7}$$

Equation S8

$$\Delta\mu_{mix} = (\mu^0 + RT\ln X_1) - (\mu^0 + RT\ln X_2) \tag{8}$$

Equation S9

$$\Delta\mu_{mix} = (\mu^0 + RT\ln\frac{X_1}{X_2}) \tag{9}$$

Where chemical potential μ_i is chemical potential, and $\Delta\mu_{mix}$ is chemical potential difference. T is the corresponding temperature, and μ_0 is a constant related to the element type. R is a constant, equal to 8.314 J/K·mol.

References

1 L. Zhang, H. Xin, D. Zhao, Z. Li and S. Ma, *Front. Mater.*, DOI:10.3389/fmats.2022.849051.

2 X. W. Zhou, R. A. Johnson and H. N. G. Wadley, *Phys. Rev. B*, 2004, **69**, 144113.

3 O. R. Deluigi, R. C. Pasianot, F. J. Valencia, A. Caro, D. Farkas and E. M. Bringa, *Acta Mater.*, 2021, **213**, 116951.

4 A. Stukowski, *Model. Simul. Mater. Sci. Eng.*, 2010, **18**, 15012.

5 H. T. Chowdhury, T. N. Palleda, N. Kakuta and K. Kakehi, 2024, DOI: 10.3390/thermo4010005.

6 X. Zhang, B. Tang, J. Li and H. Kou, ed. Y. Han, Springer Singapore, Singapore, 2019, pp. 495–503.

7 K. Hu, J. Huang, Z. Wei, Q. Peng, Z. Xie, B. Sa and B. Wu, *Phys. status solidi*, 2017, **254**, 1600634.

8 L. Zhang, P. Li, S. Li, F. Nie, B. Wu, C. Li, J. Li, Z. Zhang, X. Jiang, B. Zhao and H. Dong, *Compos. Part B Eng.*, 2024, **274**, 111288.

9 G. Petzow, E. T. Henig, H. L. Lukas, F. Aldinger and A. Prince, *Bull. Alloy Phase Diagrams*, 1980, **1**, 36–40.

10 P. Li, S. Wang, Y. Xia, X. Hao and H. Dong, *J. Mater. Sci. Technol.*, 2020, **45**, 59–69.

11 B. Wu, H. Dong, P. Li, Y. Ma, Y. Yang, C. Zou and C. Li, *J. Mater. Process. Technol.*, 2022, **305**, 117595.

12 P. Li, C. Li, H. Dong, B. Wu, Y. Ma, C. Zou and Y. Yang, *J. Alloys Compd.*, 2022, **909**, 164698.

13 P. Wang, W. Shi, L. Gu, H. Ran, Z. Pan, Y. Su, X. Song, J. Cao, H. Chen and W. Li, *J. Mater. Sci. Technol.*, 2026, **244**, 46–59.